J|A|C|S
ARTICLES
Published on Web 05/19/2006

Electrostatic-Gated Transport in Chemically Modified Glass Nanopore Electrodes

Gangli Wang, Bo Zhang, Joshua R. Wayment, Joel M. Harris,* and Henry S. White*

Contribution from the Department of Chemistry, University of Utah, 315 South 1400 East, Salt Lake City, Utah 84112

Received February 26, 2006; E-mail: white@chem.utah.edu

Abstract: Electrostatic-gated transport in chemically modified glass nanopore electrodes with orifice radii as small as 15 nm is reported. A single conical-shaped nanopore in glass, with a ~1 μm radius Pt disk located at the pore base, is prepared by etching the exposed surface of a glass-sealed Pt nanodisk. The electrochemical response of the nanopore electrode corresponds to diffusion of redox-active species through the nanopore orifice to the Pt microdisk. Silanization of the exterior glass surface with $Cl(Me)_2Si(CH_2)_3CN$ and the interior pore surface with $EtO(Me)_2Si(CH_2)_3NH_2$ introduces pH-dependent ion selectivity at the pore orifice, a consequence of the electrostatic interactions between the redox ions and protonated surface amines. Nanopore electrodes with very small pore orifice radii (< ~50 nm) display anion permselectivity at pH < 4, as demonstrated by electrochemical measurement of transport through the pore orifice. Ion selective transport vanishes at pH > 6 or when the pore radius is significantly larger than the Debye screening length, consistent with the observed ion selectivity resulting from electrostatic interactions. The ability to introduce different surface functionalities to the interior and exterior surfaces of glass nanopores is demonstrated using fluorescence microscopy to monitor the localized covalent attachment of 5- (and 6)-carboxytetramethylrhodamine succinimidyl ester to interior pore surfaces previously silanized with $EtO(Me)_2Si(CH_2)_3NH_2$.

Introduction

Molecular transport mechanisms in individual pores (e.g., protein ion channels[1] and synthetic channels[2,3]) and in materials containing pores of nanometer dimensions (e.g., zeolite catalysts[4] and skin[5]) are of interest throughout chemistry and biology. It is generally recognized that transport selectivity, based on a chemical or physical property of the permeant, is often observed in pores when the size of the pore is sufficiently small that interactions between the pore surface and permeant influence local transport dynamics. The rate of alkali metal ion transport through gramicidin channels, for instance, is highly dependent on metal ion radius, a consequence of the channel radius (~2 Å) being comparable to the dehydrated ion radius.[6] Longer range interactions over a few to tens of nanometers (e.g., electrostatic forces) between the pore surface and permeant can also lead to transport selectivity in pores of larger dimensions.[7]

Developments over the past several decades in understanding pore transport mechanisms and the origins of transport selectivity have led to recent interest in the development of chemical and biological sensors based on selective transport through nanometer scale channels and pores. Protein ion channels, such as α-hemolysin, engineered or chemically modified to interact with a target analyte, are capable of detecting individual molecules by measuring the modulation of ionic current through the protein upon analyte binding.[8] The ability to observe molecule or particle transport dynamics within individual nanopores, rather than ensembled averaged results, has motivated fundamental research on pores employing biological as well as synthetic affinity pairs.[9]

In addition to biological pores, there have been significant advances in analytic detection employing synthetic pores in recent years, made largely possible by the rapid developments

(1) (a) Kasianowicz, J. J.; Brandin, E.; Branton, D.; Deamer, D. W. *Proc. Natl. Acad. Sci. U.S.A.* **1996**, *93*, 13770. (b) Bayley, H.; Cremer, P. S. *Nature* **2001**, *413*, 226. (c) Gu, L.-Q.; Braha, O.; Conlan, S.; Cheley, S.; Bayley, H. *Nature* **1999**, *398*, 686.

(2) (a) Ito, T.; Sun, L.; Crooks, R. M. *Anal. Chem*. **2003**, *75*, 2399. (b) Ito, T.; Sun, L.; Henriquez, R. R.; Crooks, R. M. *Acc. Chem. Res*. **2004**, *37*, 937. (c) Hinds, B. J.; Chopra, N.; Rantell, T.; Andrews, R.; Gavalas, V.; Bachas, L. G. *Science* **2004**, *303*, 62. (d) Majumber, M.; Chopra, N.; Hings, B. J. *J. Am. Chem. Soc*. **2005**, *127*, 9062.

(3) (a) Li, J.; Gershow, M.; Stein, D.; Brandin, D.; Golovchenko, J. A. *Nat. Mater*. **2003**, *2*, 611. (b) Li, J.; Stein, D.; McMullan, C.; Branton, D.; Aziz, M. J.; Golovchenko, J. A. *Nature* **2001**, *412*, 166.

(4) (a) Kortunov, P.; Vasenkov, S.; Karger, J.; Valiullin, R.; Gottschalk, P.; Fe Elia, M.; Perez, M.; Stocker, M.; Drescher, B.; McElhiney, G.; Berger, C.; Glaser, R.; Weitkamp, J. *J. Am. Chem. Soc.* **2005**, *127*, 13055. (b) Krishna, R.; van Baten, J. M. *J. Phys. Chem. B.* **2005**, *109* 6386. (c) Karger, J.; Ruthven, D. M. *Diffusion in Zeolites and Other Microporous Solids*; Wiley & Sons: New York, 1992. (d) Karger, J.; Vasenkov, S.; Auerbach, S. M. Diffusion in Zeolites. In *Handbook of Zeolite Science and Technology*; Auerbach, S. M., Carrado, K. A., Dutta, P. K., Eds.; Marcel Dekker: New York, Basel, 2003; pp 341−423.

(5) (a) Uitto, O. D.; White, H. S. *Pharm. Res*. **2003**, *20*, 646. (b) Bath, B. D.; Scott, E. R.; Phipps, J. B.; White, H. S. *J. Pharm. Sci.* **2000**, *18*, 1537. (c) Pikal, M. J.; Shah, S. *Pharm. Res*. **1990**, *7*, 213. (d) Pikal, M. J. *Adv. Drug Delivery Rev*. **2001**, *46*, 281. (e) Marro, D.; Kalia, Y. N.; Delgado-Charro, M. B.; Guy, R. H. *Pharm. Res.* **2001**, *18*, 1709.

(6) (a) Andersen, O. S.; Feldberg, S. W. *J. Phys. Chem.* **1996**, *100*, 4622. (b) Andersen, O. S. *Biophys. J.* **1983**, *41*, 147. (c) Andersen, O. S. *Biophys. J.* **1983**, *41*, 135.

(7) (a) Daiguji, H.; Yang, P.; Majumdar, A. *Nano Lett.* **2004**, *4*, 137. (b) Karnik, R.; Fan, R.; Yue, M.; Li, D.; Yang, P.; Majumdar, A. *Nano Lett*. **2005**, *5*, 943.

(8) Meller, A. *J. Phys.: Condens. Matter* **2003**, *15*, R581.

(9) Umezawa, Y.; Aoki, H. *Anal. Chem.* **2004**, *76*, 320A.

in methods and materials for nanoscale synthesis.[10−12] For example, polycarbonate membranes that contain nanosize channels have been employed for the template synthesis of gold nanotubes, which can be subsequently functionalized for biosensor applications,[10] including the detection of DNA molecules.[13] The pH-switchable ion transport selectivity has been achieved by attachment of cysteine at the surface of the Au nanotubes.[14] Solid-state nanopores fabricated in Si_3N_4 membranes[11] have been used for single molecule DNA sequencing and identification, and silicon nanotubes have been integrated with microfluidic systems for DNA sensing.[12] Carbon nanotubes (CNTs) have been employed as a nanoparticle Coulter counter.[2a] Aligned and chemically modified CNTs, incorporated into polymer films to created multichannel membrane structures, are also capable of reporting analyte binding.[2b,d]

Our laboratory recently reported the fabrication and electrochemical behavior of the glass nanopore electrode[15] comprising a Pt microdisk electrode sealed at the bottom of a conical-shaped pore in glass. The orifice of the pore can be varied between 5 and 100 nm. In contrast to pores based on free-standing membranes, a nanopore electrode is open to solution through a single orifice. As previously discussed, the advantages of this design include simplicity and reproducibility of fabrication, a built-in signal transduction element (the Pt electrode) for monitoring molecular transport through the pore, and mechanical robustness of the solid electrode (in contrast to a membrane mounted in a diffusion cell, which is a frequent method of studying transport in pores).[15]

Due to the conical shape of the pore, transport of redox molecules from the bulk solution to the electrode surface is largely determined by the solution resistance in the vicinity of the pore orifice. This geometry-based localization of the pore resistance to the orifice[15a,16] suggests that transport selectivity can be achieved by chemical modification of the interior glass surface near the pore orifice. Martin and co-workers have demonstrated this principle in the recent detection of single porphyrin molecules in a conical-shaped nanopore in a polymer membrane.[17] Two additional advantages are associated with the conical-shaped pores. First, higher ionic conductivity can be achieved with conical-shaped pores relative to cylindrical pores without sacrificing the ability to localize the resistance to the pore orifice.[18] Second, the steady-state flux of molecules (or ionic conductivity) in a long conical-shaped pore *is independent of the pore depth* for pores that have a length >20 times the orifice radii.[15a] This characteristic is potentially very important in the fabrication of nanopores that exhibit reproducible behavior.

Scheme 1

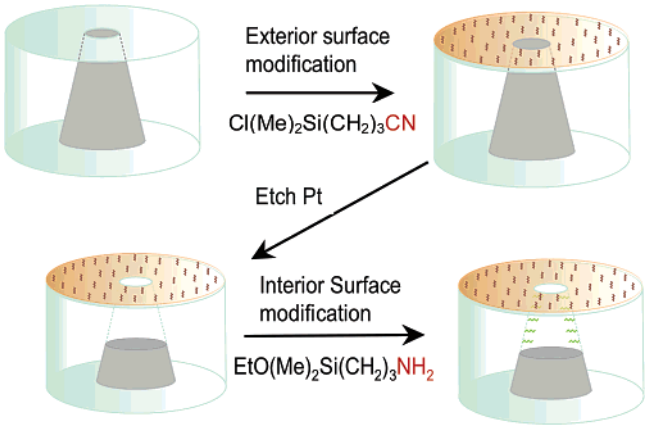

Our approach to synthesizing a nanopore electrode that exhibits transport selectivity (and, thus, also electrochemical reaction selectivity) is depicted in Scheme 1. The glass surface of a Pt nanodisk electrode (which is fabricated by sealing a sharp Pt wire in glass and polishing the glass to expose a disk) is first protected by covalent attachment of an alkanesilane that possesses a terminal "inert" functionality. The purpose of inert terminus of this monolayer is to prevent binding or specific interaction of permeants and analytes with the exterior surface of the electrode. The exposed Pt is then electrochemically etched to produce a pore that is micrometers in depth and which results in a Pt microdisk at the pore base. The Pt microdisk serves as the electrical signal transducer for electrochemical or conductivity measurements. The interior surface of the glass pore is then modified to introduce binding sites or chemical functionality that responds to external stimuli. In Scheme 1, the attachment of a $-NH_2$ terminating silane is shown, as the amine group is a convenient starting point for coupling to analyte-specific ligands.

In the present report, we demonstrate the chemical modification of glass nanopores to introduce different chemical functionality on the interior and exterior pore surface. We also show that the surface charge of the pore interior can be controlled through acid/base chemistry of the interior $-NH_2$ terminating silanes, leading to pH-gated permselectivity in individual nanopores based on electrostatic interactions.

Experimental Section

Chemicals. Bis(cyclopentadienyl)iron (ferrocene, Fc), hexaammineruthenium(III) chloride ($Ru(NH_3)_6Cl_3$), potassium hexacyanoferrate(II) hydrate ($K_4Fe(CN)_6 \cdot 3H_2O$) (all from Strem Chemicals, Inc.), 5- (and 6)-carboxytetramethylrhodamine succinimidyl ester (Biotum Inc.), 3-cyanopropyldimethylchlorosilane ($Cl(Me)_2Si(CH_2)_3CN$), and 3-aminopropyldimethylethoxysilane ($EtO(Me)_2Si(CH_2)_3NH_2$) (Gelest Inc.) were used as received. Aqueous solutions were prepared using 18 MΩ·cm water from a Barnstead E-pure water purification system. Acetonitrile (HPLC grade, J. T. Baker) was stored over 3 Å molecular sieves.

Electrode Fabrication. Fabrication of a nanopore electrode involves four general steps as previously described:[15a] (1) electrochemically etching a small diameter Pt wire to produce a sharp tip with radius of curvature of ~10 nm; (2) sealing the sharpened Pt tip into a glass capillary; (3) polishing the capillary until a Pt nanodisk is exposed;

(10) (a) Jirage, K. B.; Hulteen, J. C.; Martin, C. R. *Science* **1997**, *278*, 655. (b) Harrell, C. C.; Lee, S. B.; Martin, C. R. *Anal. Chem.* **2003**, *75*, 6861. (c) Harrell, C. C.; Kohli, P.; Siwy, Z.; Martin, C. R. *J. Am. Chem. Soc.* **2004**, *126*, 15646.
(11) (a) Fologea, D.; Gershow, M.; Ledden, B.; McNabb, D. S.; Golovchenko, J. A.; Li, J. *Nano Lett.* **2005**, *5*, 1905. (b) Fologea, D.; Gershow, M.; Uplinger, J.; Thomas, B.; McNabb, D. S.; Li, J. *Nano Lett.* **2005**, *5*, 1734. (c) Chen, P.; Gu, J.; Brandin, E.; Kin, Y.-R.; Wang, Q.; Branton, D. *Nano Lett.* **2004**, *4*, 2293. (d) Storm, A. J.; Chen, J. H.; Ling, X. S.; Zandbergen, H. W.; Dekker, C. *Nat. Mater.* **2003**, *2*, 537. (e) Liu, N.; Dunphy, D. R.; Atanassov, P.; Bunge, S. D.; Chen, Z.; López, G. P.; Boyle, T. J.; Brinker, C. J. *Nano Lett.* **2004**, *4*, 551.
(12) Fan, R.; Karnik, R.; Yue, M.; Li, D.; Majumdar, A.; Yang, P. *Nano Lett.* **2005**, *5*, 1633.
(13) (a) Harrell, C. C.; Kohli, P.; Siwy, Z.; Martin, C. R. *J. Am. Chem. Soc.* **2004**, *126*, 15646. (b) Heins, E. A.; Siwy, Z. S.; Baker, L. A.; Martin, C. R. *Nano Lett.* **2005**, *5*, 1824.
(14) Lee, S. B.; Martin, C. R. *Anal. Chem.* **2001**, *73*, 768.
(15) (a) Zhang, B.; Zhang, Y.; White, H. S. *Anal. Chem.* **2004**, *76*, 6229. (b) Zhang, B.; Zhang, Y.; White, H. S. *Anal. Chem.* **2006**, *78*, 477. (c) Zhang, Y.; Zhang, B.; White, H. S. *J. Phys. Chem. B* **2006**, *110*, 1768.
(16) Lee, S.; Zhang, Y.; White, H. S.; Harrell, C. C.; Martin, C. R. *Anal. Chem.* **2004**, *76*, 6108.
(17) Heins, E. A.; Siwy, Z. S.; Baker, L. A.; Martin, C. R. *Nano Lett.* **2005**, *5*, 1824.
(18) Li, N.; Yu, S.; Harrell, C. C.; Martin, C. R. *Anal. Chem.* **2004**, *76*, 2025.

and (4) electrochemically etching the exposed Pt to produce a truncated cone-shaped nanopore in glass, the bottom of the pore defined by a Pt microdisk electrode. The details of each step used in the current work are slightly different from those previously published[15] and are described in the following paragraphs.

Fabricating a nanopore in glass is limited by the initial sharpness of the Pt tip and the ability to expose a very small Pt disk by polishing the glass. The etching and polishing steps require careful attention in order to fabricate pores in glass with orifice radii less than 50 nm.

(1) Pt Tip Preparation. A 25 μm diameter Pt wire (Alfa Aesar, 99.95%), about 4 cm in length, was attached to W wire (0.01 in diameter, FHC) using Ag conductive epoxy (Dupont). The epoxy was cured at 120 °C for 15 min. The W/Pt wire was then carefully inserted into a glass capillary, W end first, leaving ~2 cm of the Pt wire out the capillary. The end of the Pt wire (~1 cm) was immersed vertically into a 15% $CaCl_2$ solution prepared from a 1:1 (v/v) mixture of H_2O and acetone. An AC voltage of 3 V was applied between the Pt tip and a larger Pt wire, resulting in vigorous bubbling at the Pt tip. The AC voltage was removed as the bubbling ceased, indicating complete etching of the wire to the solution/air interface. The sharpened Pt tips, with half-cone angles of ~9° as measured by optical microscopy, were cleaned by rinsing in H_2O, EtOH, and piranha solution. Tips prepared by this method were found by transmission electron microscopy to have radii of curvature of ~50 nm, which is too large to produce pores described in this report. The tips were thus re-sharpened by electropolishing in dilute H_2SO_4 using a modification of the procedure first described by Libioulle et al.[19] The etched Pt tip was inserted into a 0.1 M H_2SO_4 solution, and positive 15 V pulses (vs a large Pt electrode) of 16 μs duration were applied at a repeating frequency of 4 kHz for ~1 s. A −1.1 V DC voltage was then applied to the Pt wire for ~60 s to reduce any remaining surface oxide. This two-step electropolishing process was repeated three times. Pt tips with apex radii less than 20 nm, as measured by transmission electron microscopy, are obtained by this method.

(2) Sealing the Pt Tip in Glass. Soda-lime (Dagan Inc., i.d. = 0.75 mm; o.d. = 1.65 mm) and Pb-doped Corning 8161 glass (Warner Instruments Inc., i.d. = 1.10 mm; o.d. = 1.50 mm) capillaries were chosen based on their low softening temperature (700 and 604 °C, respectively) and high electrical resistance. The softening temperatures are ~1100 °C lower than the melting point of Pt (1769 °C), allowing the Pt tip to be sealed without melting. Following step (1), the W/Pt wire was pulled back into the capillary, leaving ~5 mm of glass extending past the Pt tip. The glass capillary was inserted into the center of a ceramic tube (McMASTER-CARR, 0.2 in. diameter) without touching the tube, and the outside of the ceramic tube was heated using a H_2-O_2 torch to ensure uniform heating. During heating, the glass capillary was rotated slowly by hand, allowing the softened glass to collapse around the end of the sharpened Pt wire. Approximately 3 mm of solid glass extends past the end of the Pt tip

(3) Exposing the Pt Nanodisk. The glass-sealed Pt electrodes were initially sanded using 400, 800, and 1200 grit papers until the glass gap between the Pt tip and its mirror image, viewed under an optical microscope (40X), is less than ~1 μm. The electrode was then polished on microcloth (Buehler) wetted with an aqueous slurry of 50 nm aluminum oxide power (Alfa Aesar) containing 0.1 M KCl. An electrical continuity measurement employing a simple MOSFET "on/off" switching circuit was used to determine when the DC resistance between the W wire extending from the top of the capillary and the wetted polishing cloth decreased below ~2 GΩ.[20] Polishing is immediately ceased at this point. The 2 GΩ resistance has been empirically determined to yield Pt nanodisks with electrochemically determined radii below 30 nm. Electrode radii (a) were determined at this point by measuring the diffusion-limited voltammetric current (i_d) for the oxidation of 5 mM ferrocene (Fc) in CH_3CN, using the equation $i_d = 4nFDCa$, where n is the number of electrons transferred, F is Faraday's constant, D is the diffusion coefficient of Fc (2.4×10^{-5} cm^2/s).[21] Using slightly larger electrodes (a = 75−100 nm), we have previously shown that the electrochemical measurement yields values that are within 20% of values determined by scanning electron microscopy (SEM). The smaller electrodes used in this study have not yet been successfully imaged by SEM due to image blurring when attempting to image small disks in glass. Thus, all radii reported here are "apparent" radii, corresponding to their electrochemical response.

(4) Etching the Pt Disk to Create a Pore. The Pt surfaces of the nanodisk electrodes were electrochemically etched in a 15% $CaCl_2$ solution (pH ~ 5.5) with the entire cell placed in an ultrasonic bath (Sonicor Instruments Corporation, Copiague, NY, Model #SC-40) to increase the rate of transport of the etching products out of the pore. A 5 V AC voltage was applied between the Pt nanoelectrode and a Pt wire counter. Large nanodisk electrodes (>100 nm) required significantly shorter etching times (10−20 s) than smaller nanodisk electrodes (<50 nm, 5−20 min) to generate a pore in the glass with a depth at least 20 times the pore orifice radius. The electrode was then rinsed with water.

Characterization of the Pore Geometry. The pore depth, d, is determined using simple geometrical relationships after measurement of the radius of the Pt disk embedded within the pore, a_p, the half-cone angle of the Pt wire, θ, and the radius of the Pt nanodisk, a (prior to creating the pore).[15a] Implicit in this determination is the assumption that the pore geometry faithfully reproduces the cone angle of the Pt wire and radius of the Pt nanodisk, both measured prior to electrochemical etching of the Pt wire. Verification of this assumption and examples of the analysis of pore geometries have been recently presented in several reports.[15] Values of a_p are determined from the voltammetric response at scan rates sufficiently large that the voltammetric current becomes limited by planar diffusion of redox molecules initially present in the pore.[15a] In this limit, the voltammetric behavior exhibits a planar diffusional response, identical to that of a macroscopic planar electrode. The value of a_p is determined from the slope of a plot of the voltammetric peak current, i_p, versus the square root of scan rate, $\nu^{1/2}$, using the expression for i_p at a shielded planar electrode under diffusion control:[22]

$$i_p = 2.69 \times 10^5 \, n^{3/2} D^{1/2} C^* \nu^{1/2} \pi a_p^2$$

Surface Modification of Nanopore Electrodes. The general strategy for silanization of the exterior and interior glass surfaces with two alkylsilanes containing different terminal groups is depicted in Scheme 1. Following exposure of a Pt nanodisk (step 3, above), the electrode was thoroughly cleaned by sonication in H_2O, EtOH, CH_3CN, and H_2O again and then soaked in 1 M HNO_3 for 10 min. The electrode was rinsed with H_2O and CH_3CN and then immersed overnight in an CH_3CN solution containing ~2% v/v $Cl(Me)_2Si(CH_2)_3CN$. The electrode was rinsed with CH_3CN and H_2O, and the Pt disk was electrochemically etched to produce the nanopore (step 4, above). Exposure of the electrode to the aqueous $CaCl_2$ solution does not remove the CN-terminated silane monolayer, as will be demonstrated below. The nanopore electrode was rinsed with H_2O and CH_3CN, and the interior glass surface was modified in an CH_3CN solution containing ~2% v/v $EtO(Me)_2Si(CH_2)_3NH_2$ using the above procedure. To ensure a complete monolayer, nanopore electrodes with orifice radii smaller than 100 nm were immersed in the $EtO(Me)_2Si(CH_2)_3NH_2$ solution for 48 h, with brief sonication at ~12 h intervals to enhance exchange of the solution constituents between the pore and external solution. Shorter immersion times (e.g., 1 h) did not result in significant attachment of the silane to the interior surface, as demonstrated by both electrochemical and

(19) Libioulle, L.; Houbion, Y.; Gilles, J.-M. *Rev. Sci. Instrum.* **1995**, *66*, 97.
(20) Zhang, B.; Galusha, J.; Wang, G.; White, R. J.; Ervin, E. N.; Cauley, C. C.; White, H. S.; Bergren, A. J. Manuscript in preparation.
(21) Kuwana, T.; Bubitz, D. E.; Hoh, G. *J. Am. Chem. Soc.* **1960**, *82*, 5811.
(22) Bard, A. J.; Faulkner, L. R. *Electrochemical Methods*, 2nd ed.; John Wiley & Sons: New York, 2001.

fluorescence measurements described below. The modified electrodes were sonicated in CH_3CN, EtOH, and H_2O to remove excess silane and then stored in H_2O. After surface modification, the electrodes could be employed in electrochemical measurements of a single solvent/redox couple for months. However, extended use of the electrode using different solvents or with different redox couples often leads to irreproducible behavior, presumably due to the adsorption and/or incomplete exchange of species within the pore.

Electrochemical Measurements. A Cypress model EI-400 bipotentiostat was interfaced to a computer through an AT-MIO16E-10 or a PCI 6251 data acquisition board (National Instruments). Voltammetric data were recorded using in-house virtual instrumentation written in LabVIEW (National Instrument). The high-sensitivity preamplifier (0.1−10 nA/V) of the bipotentiostat was used in all experiments. A one-compartment, two-electrode cell was employed with the cell and preamplifier in a Faraday cage. Typically, $I-V$ data were collected at 10^4 s^{-1} and averaged over 10^3 points, yielding noise levels less than 200 fA and a voltage resolution of 2 mV for scan rates of 20 mV/s. A Ag/AgCl electrode was used as the reference/auxiliary electrode.

Optical Microscopy. Bright-field and fluorescence microscopies were performed with the setup reported previously.[23] Briefly, the excitation source is a Spectra-Physics Model 165 argon ion laser tuned to the 514.5 nm line. The laser beam is first passed through a Pellin−Broca prism and apertured to remove plasma lines. The beam is collimated and then passed through a $^1/_4$ wave plate to convert the plane-polarized radiation into circularly polarized light. The beam is then passed through a roughened glass disk, rotated at several hundred rpm, to average out the speckle pattern on the time scale of the experiment and to create an incoherent spot source for excitation. The spot is re-imaged with a 55 mm focal length, *f*/1.2 camera lens (Canon) into the back of an inverted microscope (Nikon TE200) in order to overfill the collection cone of the objective, creating a nearly uniform intensity profile over the observation area. The objective used is a Nikon Plan Fluor 100X, 1.3 NA, infinity-corrected oil immersion lens with 0.20 mm working distance. Images are collected back through the same objective and pass through the dichroic beam splitter and a 530 nm long pass emission filter (Chroma). The cooled CCD camera (Photometrics) is controlled using Meta imaging software (Universal Imaging Corp.)

Results and Discussion

The ability to chemically modify the exterior and interior pore surfaces with silanes terminating in different functional groups was demonstrated by selective covalent attachment of a highly fluorescent probe molecule to $-NH_2$ sites on the interior glass surface of several pore electrodes, followed by fluorescence microscopy to demonstrate the spatially localized attachment of the probe molecule. Following the procedure depicted in Scheme 1, the exterior glass surface was first reacted with $Cl(Me)_2Si(CH_2)_3CN$ (see Experimental Section) to generate a silane monolayer terminating in a $-CN$ group. The Pt disk electrode was then electrochemically etched in $CaCl_2$ to produce a pore and the newly exposed interior glass surface silanized in an CH_3CN solution containing $EtO(Me)_2Si(CH_2)_3NH_2$ to yield a monolayer terminating in a $-NH_2$ group.

The underlying assumption of the above strategy is that the $-CN$ terminal monolayer created prior to pore formation protects the outer glass surface against further reaction with the amine silane. To confirm the ability to place different functional groups on the exterior and interior surfaces, the electrode was immersed in an CH_3CN solution containing 1 μM 5- (and 6)-carboxytetramethylrhodamine succinimidyl ester (TMR-SE), leading to covalent attachment of the rhodamine derivative to surface amine groups via amide bond formation. The chemically modified electrodes were thoroughly rinsed with CH_3CN and MeOH to remove any unbound rhodamine dye.

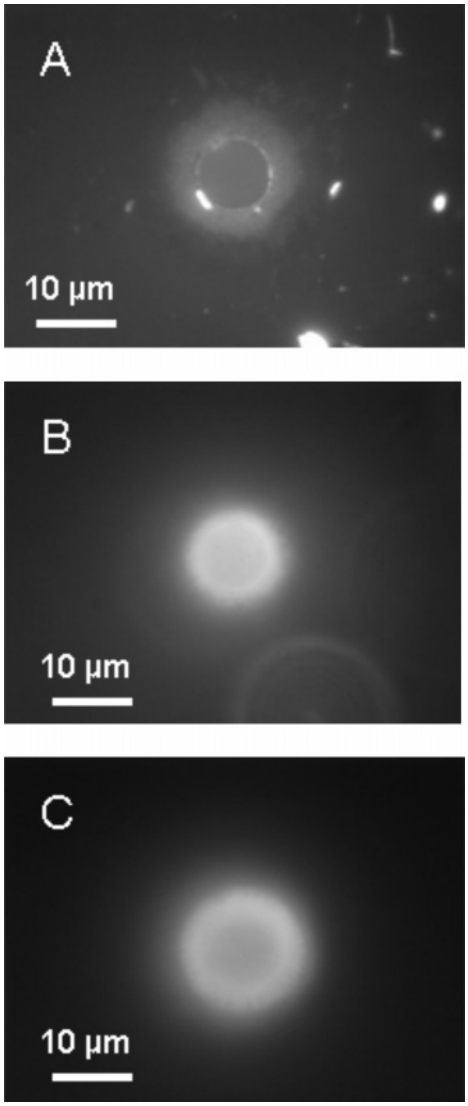

Figure 1. Fluorescence images of a micropore electrode (4 μm orifice radius, ~20 μm deep) immersed in methanol. The exterior glass surface is modified with $Cl(Me)_2Si(CH_2)_3CN$ and the interior pore surface with $EtO(Me)_2Si(CH_2)_3NH_2$, followed by covalent attachment of 5- (and 6)-carboxytetramethylrhodamine succinimidyl ester to $-NH_2$ groups on the interior pore glass surface. Images A, B, and C correspond, respectively, to fluorescence collected at focal planes located approximately at the top, middle, and bottom of the pore.

Figure 1 shows fluorescence images (in methanol) of a micropore electrode that has a ~4 μm radius orifice, as determined from the voltammetric limiting current of the corresponding disk electrode prior to creating the pore (see Experimental Section). The use of a pore electrode with a relatively large orifice allows the pore structure to be resolved by optical microscopy, which is not feasible for the nanopore electrodes with orifice radii smaller than the optical diffraction limit. Fluorescence images at different depths within the electrode (Figure 1) were obtained by scanning the microscope focal plane from the top exterior glass surface to the bottom of the pore. Fluorescence is collected within ±1 μm of the focal plane.

(23) (a) McCain, K. S.; Hanley, D. C.; Harris, J. M. *Anal. Chem.* **2003**, *75*, 4351. (b) Hanley, D. C.; Harris, J. M. *Anal. Chem.* **2001**, *73*, 5030.

Image A in Figure 1 was taken with the focal plane at the exterior glass surface. A few bright spots are observed on the exterior surface that correspond to fluorescence from surface defects or adsorbed particles. The circular band of low-intensity fluorescence in the image center corresponds to rhodamine dye bound to the interior surface near the pore orifice (the ~4 μm radius orifice is clearly evident in the image). As the focal plane of the microscope is scanned to depths within the pore interior, both the fluorescence intensity (image B) and the diameter of the bright ring increase (image C), the latter resulting from the conical shape of the pore. Images B and C are taken at focal planes located at ca. 5 and 9 μm from the exterior glass surface, corresponding approximately to the middle and the bottom of the pore. The sequence of images in Figure 1 confirms that the fluorescent rhodamine dye is immobilized via covalent bonding to the $-NH_2$ silane monolayer on the interior wall.

In control experiments, micropore electrodes of orifice radii between 1 and 10 μm that were not chemical modified, or those modified with the $-$CN silane on *both* the exterior and interior surfaces, did not show fluorescence after exposure to the rhodamine solution under the same reaction conditions as above. Conversely, fluorescence images of micropore electrodes modified with the $-NH_2$ silane on both the exterior and interior surface, followed by exposure to the rhodamine solution, showed strong fluorescence intensity from both interior and exterior glass surfaces.

Figure 2 shows bright-field (A and B) and fluorescence (C and D) images of a nanopore electrode with a 30 nm radius orifice. The bright-field images correspond to illumination from behind the electrode, in a direction approximately parallel to the glass capillary. Images A and C were taken with the microscope focal plane at the exterior glass surface, while images B and D were obtained with the focal plane at the pore base, near the Pt surface.

The bright spot in the bright-field image of the external surface (image A) results from refraction of light at the glass/methanol solution interface within the pore and subsequent emission from the pore orifice. The light focusing effect is also observed in the bright-field images of the larger pores but appears as a ring of bright intensity along the pore circumference (see Supporting Information). The shadow in the bottom right of the image is due to the Pt wire. The fluorescence image taken at the same focal plane (image C) also displays a bright spot, resulting from rhodamine fluorescence at the interior pore walls. The bright spots in the bright-field and fluorescence images appear at the same position and have a size of ~0.3 μm, corresponding to the optical diffraction limit. The fluorescence image again demonstrates that the covalent attachment of the rhodamine dye is localized to the pore interior.

The bright-field image obtained at the focal plane near the bottom of the pore displays a ~1 μm diameter black disk, a consequence of the Pt wire blocking the light. The corresponding fluorescence image shows a weak bright disk with ~0.8 μm diameter. The distance between the optical focal planes at the top and bottom of the pore was estimated to be ~6 $\pm$ 2 μm, in reasonable agreement with a ~9 μm pore depth determined from electrochemical measurements (see Experimental Section).

pH-Controlled Electrostatic-Gated Transport in the Nanopore. As discussed in the Introduction, mass transfer rates within the glass nanopore are largely determined by the resistance of the orifice.[15a] Any significant change in this local resistance is reflected in a corresponding change in the transport-limited voltammetric current. The results presented here demonstrate that mass transport of a charged species through the pore can be electrostatically gated "on" and "off" by controlling the electrical charge density at the orifice via the reversible protonation of the $-NH_2$ groups bound to pore inner surface.

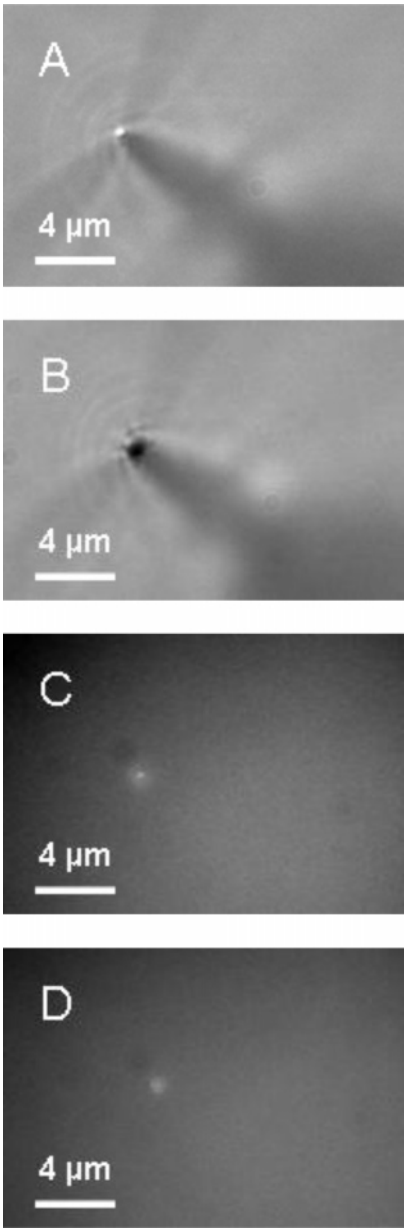

Figure 2. Bright-field (A and B) and fluorescence images (C and D) of a nanopore electrode (~30 nm radius orifice), immersed in methanol, following attachment of 5- (and 6)-carboxytetramethylrhodamine succinimidyl ester to $-NH_2$ groups on the silanized interior pore surface (see Figure 1 caption). Images A and C correspond to the pore orifice, while images B and D correspond to the pore bottom.

Figure 3 shows two examples of the pH-dependent electrochemical behavior of glass nanopore electrodes following chemical modification of the exterior glass surface with $Cl(Me)_2Si(CH_2)_3CN$ and the interior pore surface with $EtO(Me)_2Si(CH_2)_3NH_2$. In these experiments, the voltammetric response (scan rate = 20 mV/s) corresponding to the 1-e reduction of $Ru(NH_3)_6^{3+}$ (5 mM, without supporting

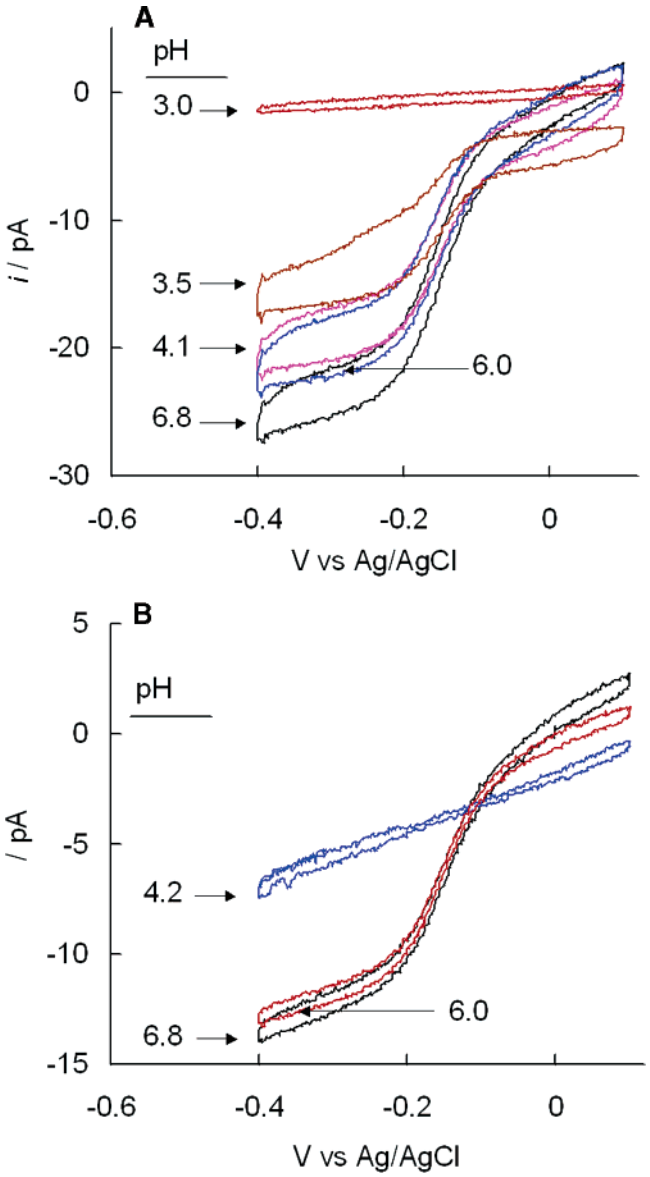

Figure 3. The pH dependence of the voltammetric response in the absence of supporting electrolyte of (A) 30 nm radius and (B) 15 nm radius nanopore electrodes in a 5 mM $Ru(NH_3)_6Cl_3$ aqueous solution following silanization of the exterior glass surface with $Cl(Me)_2Si(CH_2)_3CN$ and the interior nanopore surface with $EtO(Me)_2Si(CH_2)_3NH_2$. The pH was varied from neutral to low pH and back to neutral (pH = 6.8, 4.1, 3.5, 3.0, and 6.0 in A, and pH = 6.8, 4.2, 4.1, and 6.0 in B).

electrolyte) was recorded over a pH range between ~3 and ~7 for nanopore electrodes with radii of 30 (Figure 3A) and 15 nm (Figure 3B). The solution pH was varied by addition of small volumes of HCl and NaOH.

At pH > 6, the voltammetric responses of the modified electrodes display a quasi-sigmoidal voltammogram with $E_{1/2}$ ~ −0.15 V vs Ag/AgCl that corresponds to the transport-controlled reduction of $Ru(NH_3)_6^{3+}$. (In the absence of supporting electrolyte, the flux of $Ru(NH_3)_6^{3+}$ to any electrode contains a minor migrational component.[24] Thus, we refer to "transport-controlled" rates rather than "diffusion-controlled" rates.) Several recent reports from this laboratory have demonstrated that the shape of the voltammetric wave for the nanopore electrodes is the same as that for the corresponding nanodisk electrodes (prior to etching the Pt to create a disk). However, the magnitude of the currents for nanopore electrodes is reduced in comparison to the current at the corresponding disk, a consequence of the increased mass transport resistance associated with the pore. For a conical-shaped nanopore electrode with $\theta = 9°$, it has been shown by theory, simulation, and experiment that the steady-state limiting current asymptotically decreases with increasing pore depth to a value that is ~20% of the corresponding nanodisk.[15a] The asymptotic limit is obtained (within 95%) when the pore depth is 20 times the orifice radius. Thus, the voltammetric current in these measurements remains a significant fraction of the value prior to creating the pore, even for very deep pores. This limiting behavior of conical-shaped pores is very advantageous in studying the influence of chemical and physical interactions on transport of through pores.

For the two glass nanopore electrodes employed in obtaining the data shown in Figure 3, the voltammetric limiting current associated with $Ru(NH_3)_6^{3+}$ reduction decreases precipitously with decreasing pH, dropping to negligible values at pH ~ 3. This decrease in the transport-limited current is not observed at the corresponding nanodisk electrode (prior to etching) and is thus ascribed to a pH-dependent mass transfer resistance of the pore. We note that the steady-state current measured at the Pt electrode located at the base of the pore is proportional to the transport rate of $Ru(NH_3)_6^{3+}$ through the pore orifice (R_{mt}, mol/s) by the relationship, $i = nFR_{mt}$. Thus, the observation, at low pH, of a negligibly small faradaic current due to $Ru(NH_3)_6^{3+}$ reduction corresponds to a negligible flux of $Ru(NH_3)_6^{3+}$ through the pore orifice. The transport-controlled flux of $Ru(NH_3)_6^{3+}$ through the pore orifice is restored by raising the pH back to ~6, as shown in Figure 3 for both 30 and 15 nm radius orifices.

The two examples of pH-controlled voltammetric currents shown in Figure 3 are qualitatively reproducible (see Supporting Information for additional examples), although the magnitude of the decrease at low pH is sometimes less than that shown in Figure 3. The voltammetric waveshapes recorded in these experiments, however, are frequently different than the ideal sigmoidal shape predicted by theory. For instance, the sloping background current in Figure 3B for the 15 nm radius pore electrode indicates a significant ohmic leakage current superimposed on the current resulting from $Ru(NH_3)_6^{3+}$ reduction. We believe that this leakage current is associated with Na^+ transport through the wall of the soda-lime glass capillary used to prepare the electrode. Such small leakage currents through soda-lime glass are observable when recording data at pA sensitivity (indeed, linear ohmic $I-V$ curves for Pt wires that are *completely sealed* in soda-lime glass capillaries can be observed at pA sensitivity, i.e., without exposing any Pt surface to the solution). Conversely, the flat baseline in Figure 3A is for an electrode prepared from Pb (~30%)-doped glass, which exhibits a much smaller ionic conductivity than that of soda-lime glass.[25]

The decrease in the voltammetric current at low pH clearly reflects an electrostatic repulsion between the protonated surface

(24) (a) Amatore, C.; Fosset, B.; Bartelt, J.; Deakin, M. R.; Wightman, M. R. *J. Electroanal. Chem.* **1988**, *256*, 255. (b) Oldham, K. B. *J. Electroanal. Chem.* **1988**, *250*, 1. (c) Zoski, C. G. In *Modern Techniques in Electroanalysis*; Vanysek, P., Ed.; Wiley: New York, 1996; p 241.

(25) Abelson, J. N.; Simon, M. I.; Rudy, B.; Iverson, L. E. *Methods in Enzymology*; Academic Press: New York, 1992; Vol. 207.

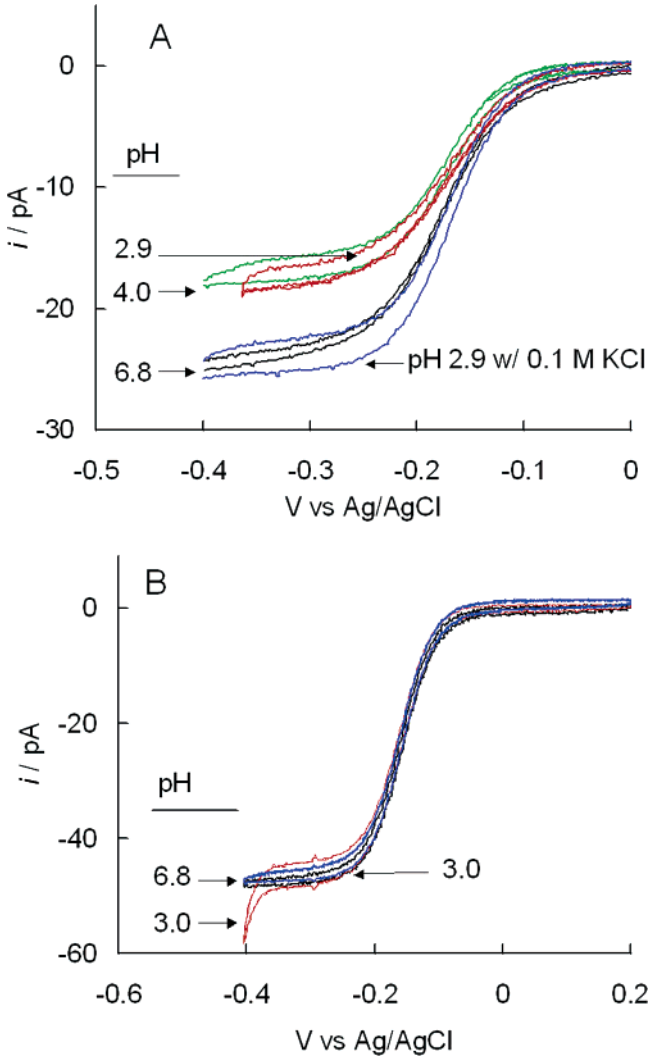

Figure 4. (A) Voltammetric response of a 25 nm radius nanopore electrode in a 5 mM $Ru(NH_3)_6Cl_3$ solution as a function of pH and electrolyte concentration. The voltammograms were recorded in the absence of electrolyte in the following order: pH = 6.8, 4.0, and 2.9, and then in the presence of 0.1 M KCl at pH = 2.9. (B) pH dependence of the voltammetric response of a 70 nm radius nanopore electrode in a 5 mM $Ru(NH_3)_6Cl_3$ solution. Both A and B correspond to electrodes with the exterior glass surface silanized with $Cl(Me)_2Si(CH_2)_3CN$ and the interior nanopore surface with $EtO(Me)_2Si(CH_2)_3NH_2$.

amines ($-NH_3^+$) and $Ru(NH_3)_6^{3+}$, preventing $Ru(NH_3)_6^{3+}$ from entering the pore.[26] The pK_a of siloxane-tethered monolayers of amines on glass are reported to be significantly lower (~3−5) than their corresponding value in bulk solution due to unfavorable electrostatic interactions between neighboring $-NH_3^+$.[27] The decrease in voltammetric current beginning at pH between 5 and 6 (Figure 3) suggests that the surface $-NH_2$ groups on the interior pore surface are initially protonated in this pH range. The voltammetric data do not allow a measurement of the surface pK_a, as no quantitative relationship between transport rates through orifices and the degree of surface ionization exists to our knowledge. Thus, the number of $-NH_3^+$ groups necessary to prevent $Ru(NH_3)_6^{3+}$ from entering the pore is unknown.

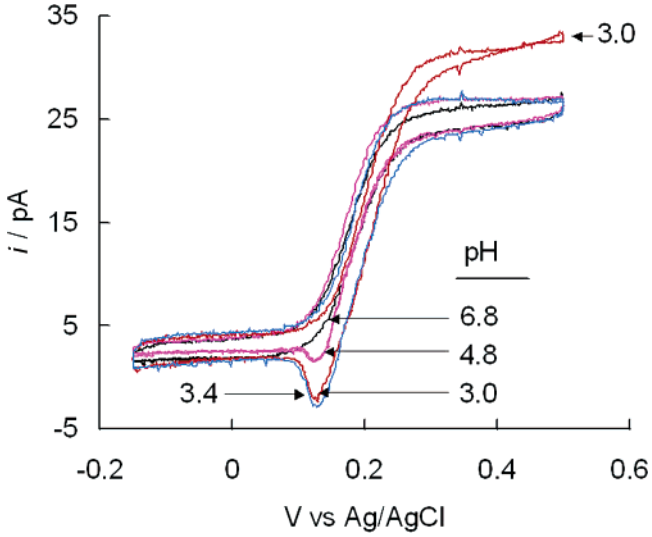

Figure 5. The pH dependence of the voltammetric response of a 30 nm radius nanopore electrode in a 5 mM $K_4Fe(CN)_6$ solution. The exterior glass surface was modified with $Cl(Me)_2Si(CH_2)_3CN$ and the interior surface of the nanopore with $EtO(Me)_2Si(CH_2)_3NH_2$. The pH was varied in the following order: 6.8, 4.8, 3.4, and 3.0.

Surface $-NH_3^+$ groups generate an electric field that points radially into the pore, filling the pore to the largest degree near the orifice where the pore radius is smallest. Assuming the electric field extends a distance of 3 κ^{-1}, where κ^{-1} is the Debye length of a 0.01 M solution (which we take as approximating the ionic strength of a 5 mM multivalent $Ru(NH_3)_6Cl_3$ solution), suggests that the field extends a distance of ~10 nm into the pore. Thus, the field extends almost entirely across the orifice of a 15 nm radius pore (Figure 3B) and over a significant fraction of a 30 nm radius pore (Figure 3A).

In principle, the key parameter in determining whether the flux of a charged species can be electrostatically gated is the ratio κ^{-1}/a, which can be varied over a wide range of values in our experiment by using glass nanopores with different radii or by adding a supporting electrolyte. Intuitively, for large pores or in solutions of high ionic strength, $\kappa^{-1}/a \rightarrow 0$, and the presence of surface $-NH_3^+$ should have little or no influence on the transport rate of $Ru(NH_3)_6^{3+}$. This prediction is experimentally observed. Figure 4A shows the voltammetric response of a 25 nm radius nanopore electrode, modified as before with interior $-NH_2$ and exterior $-CN$ terminal silanes. This electrode shows a qualitatively similar decrease in the voltammetric current for $Ru(NH_3)_6^{3+}$ when the pH is lowered, but to a lesser degree than the examples shown in Figure 3. Nevertheless, when 0.1 M KCl is added to the solution, the voltammetric current is restored to its original value measured at neutral pH. Clearly, the addition of KCl screens the electric field originating from the surface $-NH_3^+$, thereby reducing the electrostatic repulsion between $-NH_3^+$ and $Ru(NH_3)_6^{3+}$. Quantitatively, the addition of 0.1 M KCl reduces κ^{-1}/a from ~0.4 to ~0.12. Figure 4B shows the response of a chemically modified nanopore electrode with an 80 nm radius orifice in the absence of supporting electrolyte ($\kappa^{-1}/a \sim 0.13$). In this example, the pH had no effect on the voltammetric response.

The flux of a redox-active anion through the orifice of glass nanopore electrodes modified with interior $-NH_2$ groups should

(26) Electrostatic repulsion also prevents $Ru(NH_3)_6^{3+}$, initially in the pore before the pH is lowered, from leaving the pore. The number of trapped molecules can be determined by thin-layer voltammetric methods. Investigations of trapping $Ru(NH3)_6^{3+}$ and other molecules in the pore will be reported in the future.

(27) Shyue, J.-J.; De Guire, M. R.; Nakanishi, T.; Masuda, Y.; Koumoto, K.; Sukenik, C. N. *Langmuir* **2004**, *20*, 8693.

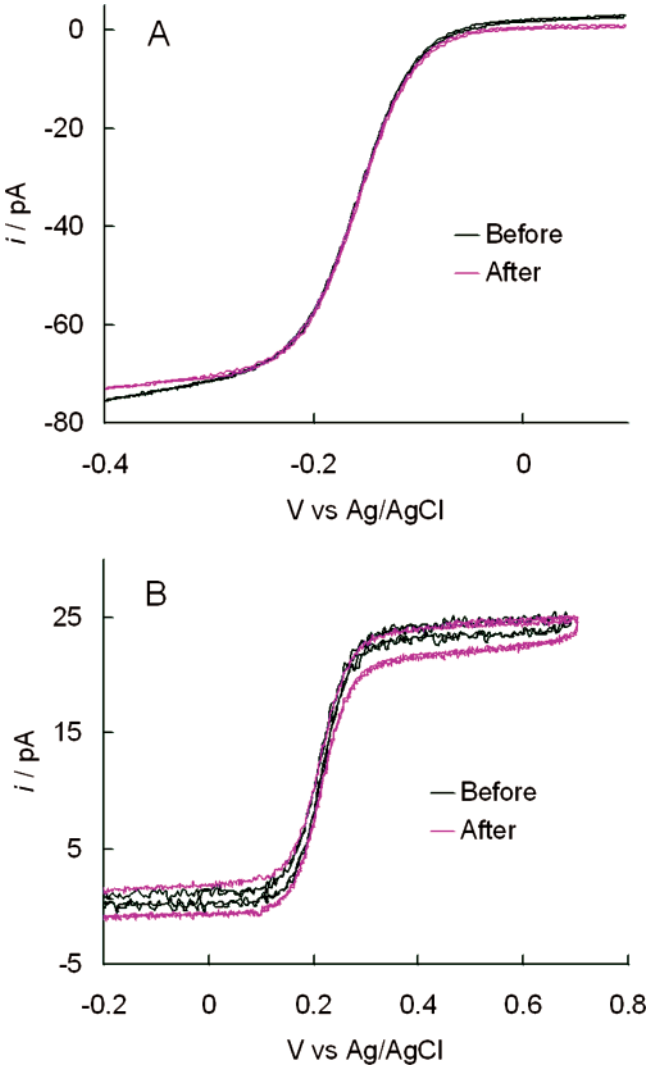

Figure 6. Voltammetric response in the absence of supporting electrolyte of a 30 nm radius Pt disk before and after silanization of the glass surfaces with $EtO(Me)_2Si(CH_2)_3NH_2$ in (A) 10 mM $Ru(NH_3)_6Cl_3$ and (B) 10 mM $K_4Fe(CN)_6$ aqueous solutions.

not decrease at low pH, as anions will be electrostatically attracted to the positive charged interior pore surface. This expectation is observed in steady-state voltammetric measurements corresponding to the 1-e oxidation $Fe(CN)_6^{4-}$. Figure 5 shows the voltammetric response of a 30 nm radius nanopore electrode in a 5 mM $K_4Fe(CN)_6$ solution, in the absence of supporting electrolyte. In contrast to the results for $Ru(NH_3)_6^{3+}$, a small *increase* in the voltammetric current is observed when the pH is lowered from pH 7 to 3, indicating an increase in the flux of $Fe(CN)_6^{4-}$ through the pore orifice when the surface is positively charged. In addition, a voltammetric peak current, corresponding to reduction of electrogenerated $Fe(CN)_6^{3-}$, appears when the pH is lowered. No such peak is detected when the pH is kept neutral. We tentatively assign the peak at low pH to electrostatic attractive interactions of electrogenerated $Fe(CN)_6^{3-}$ with $-NH_3^+$, resulting in the collection of this species within the pore during the reduction $Fe(CN)_6^{4-}$.

We note that the presence of any PtO_x on the Pt surface might result in covalent attachment of silanes to the electrode surface.[28] Silanization of the PtO_x surface with a $-NH_2$ layer would introduce permselectivity directly to the electrode,[29] erroneously masking the influence of electrostatic gating at the pore orifice. To demonstrate that the Pt surface is not chemically modified in these experiments, (unetched) Pt *nanodisk* electrodes were immersed in the CH_3CN containing $EtO(Me)_2Si(CH_2)_3NH_2$. The voltammetric responses of these electrodes were recorded, before and after chemical modification, in $Ru(NH_3)_6^{3+}$ and $Fe(CN)_6^{4-}$ solutions, both at neutral and low pH (Figure 6). No difference in the voltammetric response at pH between 3 and 7 was observed after modification of the glass, indicating the absence of a permselective layer on the Pt surface. We conclude from these experiments, and the evidence presented above, that the observed permselectivity is due to pH-adjustable electrostatic fields at the pore orifice.

Finally, unmodified glass nanopores exhibit pH-dependent permselectivity due to the deprotonation and protonation of surface $-Si-OH$ groups, acid/base chemistry that is important in more basic solutions than considered in the current report. The oxidation of $Fe(CN)_6^{4-}$ at bare 30 nm radius orifice nanopore electrodes decreases precipitously at pH $\sim$ 9 due to electrostatic repulsion between the negatively charged $-Si-O^-$ and the redox anion. No dependence of the flux of either redox cations or anions on pH was observed at pH $<$ 9 for bare glass nanopore electrodes.

Conclusions

In summary, this paper describes the chemical modification of glass nanopore electrodes to impart transport selectivity based on electrostatic forces at the pore orifice. Electrochemical detection using the relatively large Pt electrode at the base of the conical-shaped pore provides a simple but powerful means to measure the molecular interactions at the orifice of individual nanometer scale pores. We have demonstrated that the electrostatic fields at the orifice can be turned on and off by adjusting the solution pH. In qualitative agreement with classical predictions, electrostatic gating of ion flux is achieved when the electric field originating at the interior pore surface extends a distance into solution that is comparable to the orifice radius. The ability to introduce different chemical functionalities ($-CN$ and $-NH_2$ in the present report) at the exterior and interior pore surfaces should prove to be a versatile method to control the physical and chemical properties of the pore orifice, potentially introducing transport selectivity based on other types of surface–analyte interactions (e.g., biological ligand–receptor binding). We are currently pursuing this direction of research.

Acknowledgment. This research was supported by grants from the National Institutes of Health (to H.S.W.) and from the National Science Foundation (to J.M.H.).

Supporting Information Available: The bright-field image corresponding to the 4 μm radius pore electrode, and additional examples of the pH response of the nanopore electrodes. This material is available free of charge via the Internet at http://pubs.acs.org.

JA061357R

(28) Moses, P. R.; Wier, L. M.; Lennox, J. C.; Finklea, H. O.; Lenhard, J. R.; Murray, R. W. *Anal. Chem.* **1978**, *50*, 576.
(29) (a) Liu, Y.; Zhao, M.; Bergbreiter, D. E.; Crooks, R. M. *J. Am. Chem. Soc.* **1997**, *119*, 8720. (b) Hsueh, C.-C.; Brajter-Toth, A. *Anal. Chem.* **1994**, *66*, 2458. (c) Cheng, Q.; Brajter-Toth, A. *Anal. Chem.* **1996**, *68*, 4180.